



Trans. Nonferrous Met. Soc. China 29(2019) 2290-2299

Transactions of Nonferrous Metals Society of China

www.tnmsc.cn



Microstructure evolution and optimum parameters analysis for hot working of new type Mg-8Sn-2Zn-0.5Cu alloy

Li-ping ZHONG^{1,2}, Yong-jian WANG^{1,2}

College of Materials Science and Engineering,
 Sichuan University of Science and Engineering, Zigong 643000, China;
 Material Corrosion and Protection Key Laboratory of Sichuan Province,
 Sichuan University of Science and Engineering, Zigong 643000, China

Received 2 February 2019; accepted 3 July 2019

Abstract: The hot deformation behavior of as-solutionized Mg-8Sn-2Zn-0.5Cu (TZC820) alloy was investigated experimentally and numerically via isothermal compression tests at 250-400 °C and strain rate range of 0.01-3 s⁻¹ on a Gleeble-1500D thermomechanical simulator. Results show that the deformation temperature and strain rate significantly affected flow stress and material constants. In addition, the strain-compensated constitutive relationship was established on the basis of true stress-strain curves. The main deformation mechanism for this alloy was the dynamic recrystallization (DRX), and the DRX degree was effectively enhanced with an increase in deformation temperature and a decrease in strain rate. Moreover, the cellular automaton method was used to simulate the microstructure evolution during hot compression. In addition, the processing maps were established, and the optimum deformation parameters for the as-solutionized TZC820 alloy are at 370–400 °C and 0.01 s⁻¹, and at 320–360 °C and 1-3 s⁻¹.

Key words: Mg-8Sn-2Zn-0.5Cu alloy; hot deformation; dynamic recrystallization; processing map

1 Introduction

Improved mechanical properties of magnesium alloys are dramatically required given their increasing application as structural materials in the aerospace and transportation industries [1-4]. Mg-Sn based alloys, as promising low-cost and high strength wrought Mg alloys, have attracted considerable attention for several decades. However, binary Mg-Sn alloys suffer from poor age hardening response due to the existence of coarse Mg₂Sn phase [5,6]. With emphasis on the refinement of the Mg₂Sn phase, Zn has been added to a binary Mg-Sn alloy as the third element to enhance mechanical properties. The addition of Zn element results in the homogeneous distribution and refinement of Mg₂Sn precipitates, thereby increasing the number density of precipitates and promoting the formation of β precipitates on non-basal planes [7,8]. Thus, most wrought Mg-Sn-Zn based alloys can reach ultimate

tensile strength (UTS) of 300-350 MPa [9-11]. Moreover, novel Mg-Sn based alloys with a high ultimate tensile strength (UTS) of approximately 400 MPa can be prepared via state-of-art alloying design and manufacturing [12,13]. A novel as-extruded Mg-8Sn-2Zn-0.5Cu (TZC820) alloy, which exhibited a yield strength (YS) of 365.9 MPa and UTS of 388.4 MPa has been designed in our previous work [14]. The high strength is attributed to the high number density of micron-sized broken MgZnCu and Mg₂Sn particles, nano-sized Mg₂Sn precipitates and fine grains. However, the substantial interaction between α-Mg matrix and undissolved hard and brittle phases results in poor hot plasticity and even crack during hot working, thus limiting the further applications of this alloy. In the abovementioned works, dynamic recrystallization (DRX) and secondary phases significantly influence the microstructure and mechanical properties of alloys. However, the studies on Mg-Sn based alloys have mainly been focused on the alloying element addition

DOI: 10.1016/S1003-6326(19)65135-6

and improvement of mechanical properties, and the knowledge on DRX process and hot deformation behavior has not attracted sufficient attention.

Therefore, the hot deformation behavior of TZC820 alloy should be studied thoroughly to define a processing window for the stable plastic flow without cracking. This work aims to understand the hot deformation behavior of the as-solutionized TZC820 alloy under various deformation conditions. The hot deformation behaviors are characterized using hyperbolic laws in an Arrhenius type and processing map technique. In addition, the DRX behaviors are analyzed by experimental and numerical studies to validate the processing maps and reconstruct the effect of secondary phases on DRX.

2 Experimental

Cast billets were prepared from pure commercial Mg, Sn, Zn, Cu, and Mg–Mn master alloy (5 wt.%). The mixtures were melted at 750 °C in an electric resistance furnace with the protection of CO₂ and SF₆, stabilized at 700 °C for 30 min, and then poured into a steel mold pre-heated to 200 °C. The composition of the alloy is listed in Table 1.

Table 1 Chemical composition of studied alloy (wt.%)

Sn	Zn	Cu	Mn	Mg
8.33	1.78	0.48	0.16	Bal.

Furthermore, we applied progressive solution treatments to obtain a supersaturated solid solution, as illustrated in Fig. 1. Then, the as-solutionized samples were quenched in water. The cylindrical specimens were machined from an as-solutionized ingot with a height of 12 mm and a diameter of 10 mm. Hot compression was performed at 250–400 °C with strain rates of 0.01, 0.1, 1 and 3 s⁻¹ on a Gleeble–1500D thermomechanical simulator. Graphite lubricant was applied between the samples and the crosshead to reduce the deformation

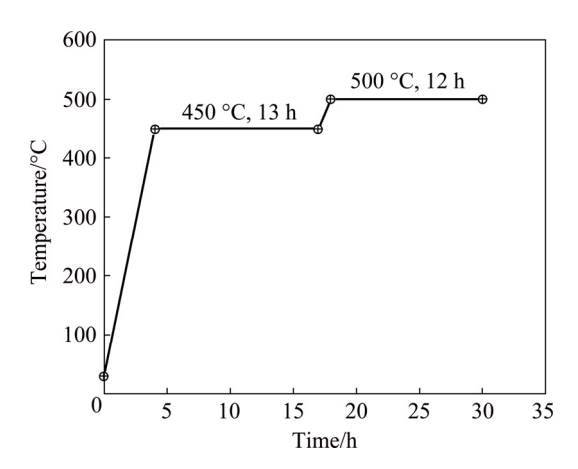


Fig. 1 Flow chart of progressive solution treatment

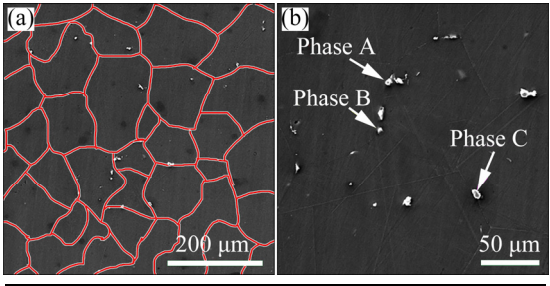
friction. The specimens were heated at a heating rate of 5 °C/s, held at a certain temperature for 2 min and then compressed to a true strain of 0.9. Deformed specimens were quenched in water immediately to maintain the deformed microstructure.

The microstructure of the as-solutionized sample was characterized using a scanning electron microscope (SEM, TESCAN VEGA II LMH) with an accelerating voltage of 20 kV equipped with an Oxford INCA Energy 350 dispersive X-ray spectrometer (EDS). Electron backscattered diffractometry (EBSD) analysis was conducted using a scanning electron microscope (JEOL 7800F) equipped with an HKL Channel 5 system operating at 20 kV. The transmission electron microscopy (TEM, Tecnai G2 F20 S-TWIN) was conducted with an operating voltage of 200 kV. TEM foils were prepared by mechanical polishing to less than 100 μm, subsequent punching into 3 mm discs and final ion-milling via a Gatan Precision Ion Polishing System (GATAN 691).

3 Results and discussion

3.1 Initial microstructure

The microstructure of the as-solutionized TZC820 alloy is depicted in Fig. 2. The average grain size is determined to be approximately 110 μ m, and a small number of undissolved particles remain in the matrix. These particles are mainly distributed along the grain



Phase	Element wt.%		at.%
	Mg	42.51	78.13
A	Sn	56.75	21.37
	Zn	0.74	0.51
	Mg	60.42	81.45
В	Zn	13.84	6.94
В	Cu	18.79	9.69
	Sn	6.95	1.92
	Mg	2.24	4.93
C	Mn	83.64	81.53
	Fe	14.12	13.54

Fig. 2 Microstructures of as-solutionized TZC820 alloy and EDS results for secondary phases

boundaries. In Fig. 2(b), three different secondary phases are marked as Phase A, Phase B and Phase C, and the EDS results indicate that the secondary particles are Mg₂Sn, MgZnCu and α -Mn, respectively. The effect of α -Mn on microstructure evolution and the mechanical properties of as-solutionized TZC820 alloy are ignored due to the relatively low content.

In accordance with the Mg–Sn and Mg–Cu binary phase diagrams, the presence of undissolved Mg₂Sn and MgZnCu particles is mainly attributed to a high content of Sn element and the limited solid solubility of Cu in the α -Mg matrix after high-temperature progressive solution treatments.

3.2 Hot deformation behavior

A series of typical true stress—strain curves obtained during hot compression for as-solutionized TZC820 alloy at various strain rates and temperatures are demonstrated in Fig. 3. Evidently, the strain rate and deformation temperature significantly affect the flow stress level. Generally, flow stress increases with a decrease in deformation temperature and an increase in strain rate. All curves sharply increase to the peak value due to work hardening and gradually decrease to a relatively steady state as a result of a balance between work hardening caused by accumulation of dislocation generation, pile-up, and tangle and dynamic softening by

dynamic recovery (DRV) and dynamic recrystallization (DRX) [15,16]. Moreover, in accordance with the feature of the curves, the alloy exhibits a feature of DRX during hot deformation [17]. Thus, the hot deformation process of the as-solutionized TZC820 alloy can be considered a competition of work hardening and DRX. Moreover, under high strain rate, the difference between the stress levels of the alloy increases with increasing deformation temperature. At low temperature (250 °C), dislocation migration is slow, and nearly no dynamic recrystallization occurs in the alloy at the strain rates of 1 and 3 s⁻¹. However, the dislocation migration is fast at high temperature (400 °C), and the degree of dynamic recrystallization of the alloy at both strain rates is significantly different, thus leading to the occurrence of this phenomenon [18].

The strain significantly affects the flow behavior of alloys during hot deformation, as shown in Fig. 3. Therefore, the strain-compensated Arrhenius equations are applied to describing the hot deformation behavior of a material and establishing the relationships among flow stress, strain, strain rate and temperature [19–21]. A strain-compensated constitutive equation can be utilized. First, the material parameters α , β , n, Q and $\ln A$ of the alloy can be obtained from the experimental data at a specific strain. For example, Fig. 4 illustrates the relationships of the material parameters of the

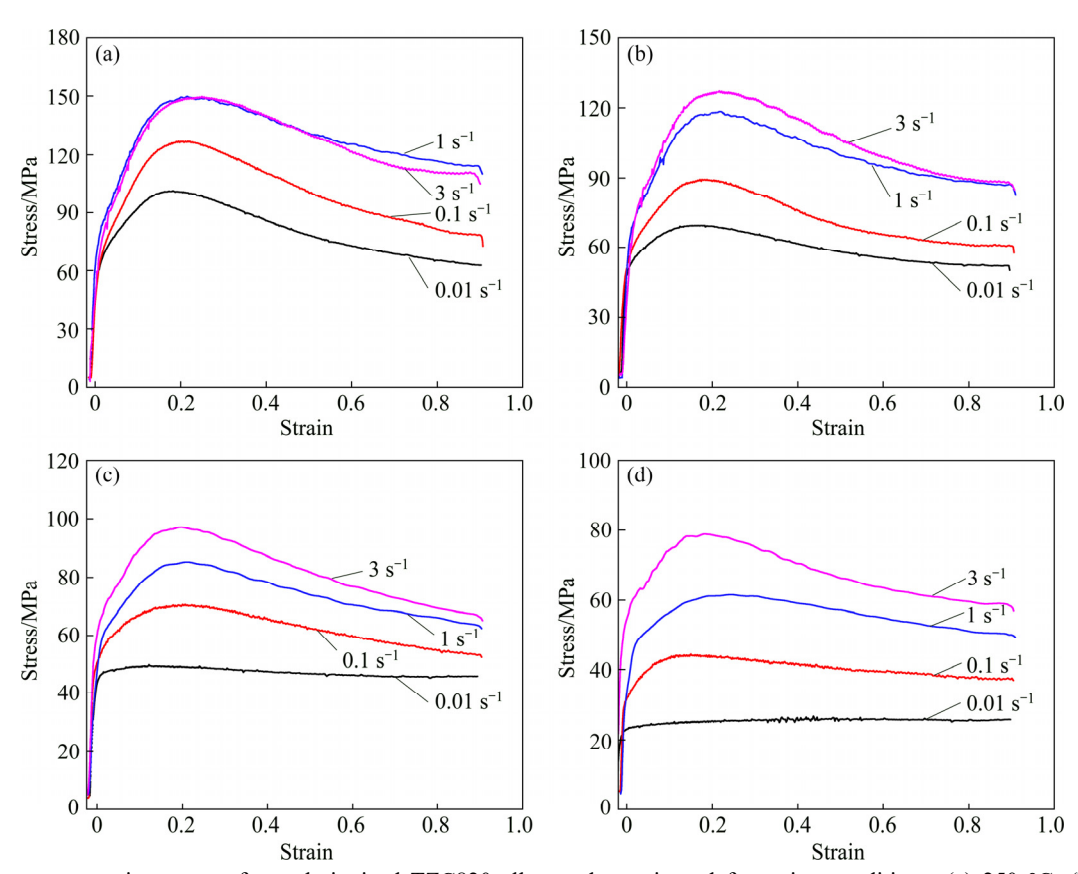


Fig. 3 True stress-strain curves of as-solutionized TZC820 alloy under various deformation conditions: (a) 250 °C; (b) 300 °C; (c) 350 °C; (d) 400 °C

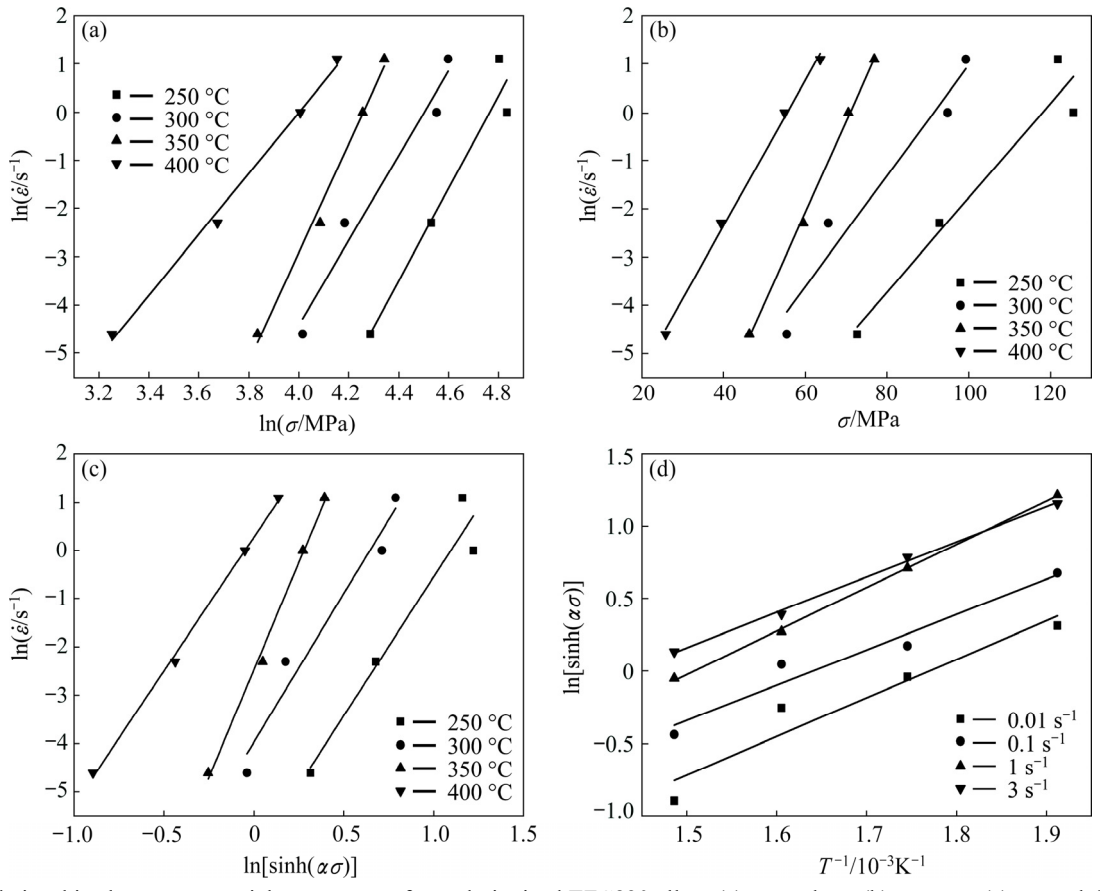


Fig. 4 Relationships between material parameters of as-solutionized TZC820 alloy: (a) $\ln \dot{\varepsilon} - \ln \sigma$; (b) $\ln \dot{\varepsilon} - \sigma$; (c) $\ln \dot{\varepsilon} - \ln[\sinh(\alpha\sigma)]$; (d) $\ln[\sinh(\alpha\sigma)] - 1/T$

as-solutionized TZC820 alloy at strain of 0.6. Moreover, the material parameters α , n, Q and $\ln A$ are evaluated as 0.0154 MPa⁻¹, 35.83, 350.58 kJ/mol and 123.06 s⁻¹, correspondingly. Second, to model the constitutive equation with strain compensation, the material constants are determined simultaneously under different strains ranging from 0.1 to 0.9 with an interval of 0.1. The relationships between the material constants and deformation strains for the as-solutionized TZC820 alloy can be fitted in a polynomial by the compensation of strain. The variation in material constants with the strain is complex. Finally, the curves of the material parameters with strain are obtained, as presented in Fig. 5.

Moreover, the relationships between strain and material constants can be described using fourth order polynomial fitting:

$$Y = X_0 + X_1 \varepsilon + X_2 \varepsilon^2 + X_3 \varepsilon^3 + X_4 \varepsilon^4 \tag{1}$$

where Y is the material parameter, X is the fitting coefficient and ε is the strain. Based on the analysis of correlation and generalization, the polynomial fitting coefficients of α , n, Q and $\ln A$ for the as-solutionized TZC820 alloy are listed in Table 2. In accordance with the expression of the hyperbolic law, the constitutive equations for the hot deformation behavior of the as-solutionized TZC820 alloy at a certain strain, strain

rate and deformation temperature can be predicted using

$$\begin{cases}
\sigma(\varepsilon) = \frac{1}{\alpha(\varepsilon)} \ln \left\{ \left(\frac{Z(\varepsilon)}{A(\varepsilon)} \right)^{1/n(\varepsilon)} + \left[\left(\frac{Z(\varepsilon)}{A(\varepsilon)} \right)^{1/n(\varepsilon)} + 1 \right]^{0.5} \right\} \\
Z(\varepsilon) = \dot{\varepsilon} \exp \left(\frac{Q(\varepsilon)}{RT} \right)
\end{cases}$$
(2)

3.3 Microstructure evolution

3.3.1 Experimental study

Figure 6 illustrates hot-compressed microstructure of the as-solutionized TZC820 alloy at various deformation temperatures and strain rates. microstructure evolution of the studied alloy closely depends on the deformation temperature and strain rate. Figure 6(a) plots an inverse pole figure (IPF) map of the sample compressed at 250 °C and 0.01 s⁻¹. It can be seen that the DRXed grains are mainly distributed around coarse deformed grains, and the crystallographic orientations are more random in the DRXed grains than in the coarse deformed grains. In Fig. 6(b), nearly no DRXed grains appear and the majority of the deformed grains are elongated at 250 °C and 3 s⁻¹. Moreover, Fig. 6(b) displays a substantial color variation caused by

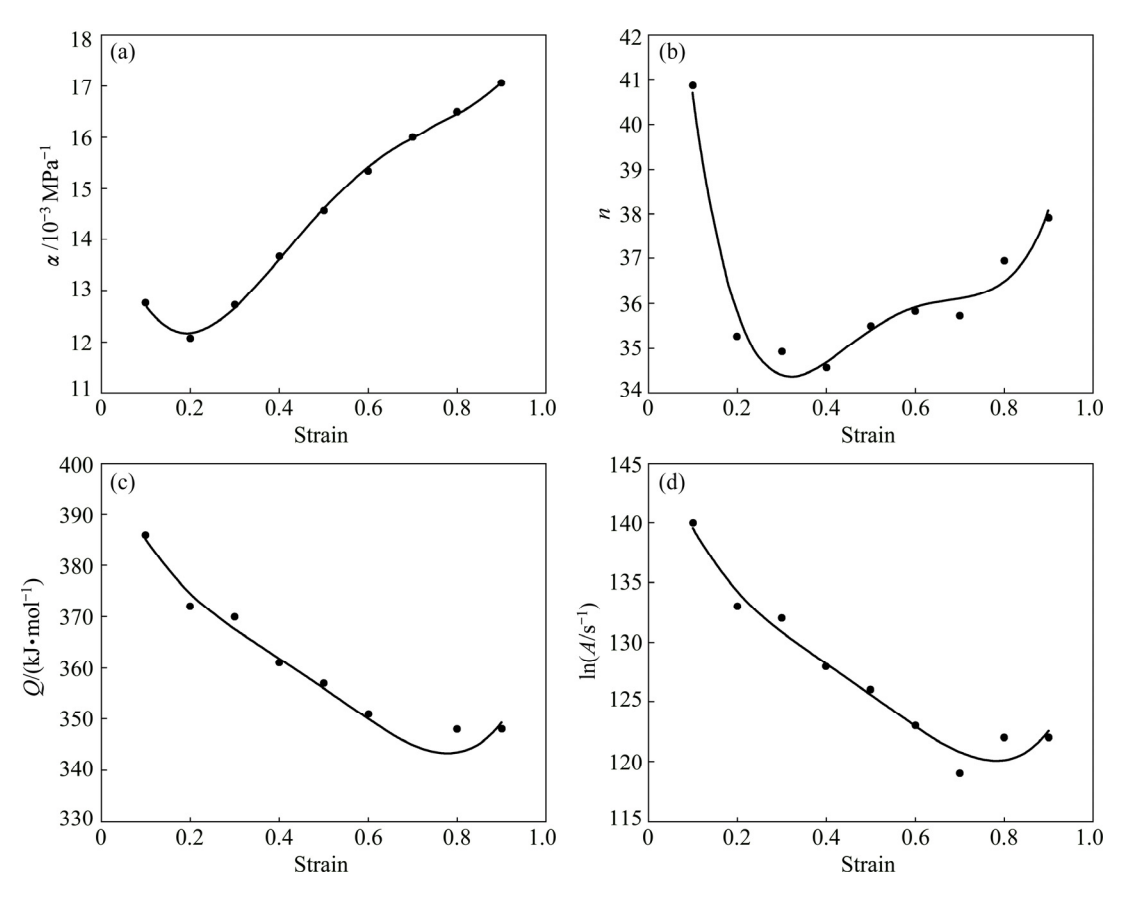


Fig. 5 Coefficients of polynomial fitting for as-solutionized TZC820 alloy: (a) α ; (b) n; (c) Q; (d) $\ln A$

Table 2 Fourth nonlinear fitting coefficients of between material parameters

Parameter	X_0	X_1	X_2	X_3	X_4
α	0.01507	-0.03525	0.13478	-0.16839	0.07212
n	54.47674	-146.45365	438.96357	-539.89468	238.41951
\mathcal{Q}	403.38889	-235.65786	626.37918	-951.30795	524.47552
$\ln A$	148.5	-114.47747	293.50233	-427.54468	230.18648

the high density of dislocations and demonstrates a dominant kink deformation in many coarse deformed grains [22]. The appearance of straight grain boundaries may be due to the limited slip system of the HCP crystal structure at low temperature. In addition, time is insufficient for migrating dislocations at a high strain rate, thus suppressing the DRX process of the as-solutionized TZC820 alloy [19]. In Fig. 6(d), when the deformation temperature increases to 400 °C, numerous new fine grains nucleate along the original boundaries of the as-solutionized TZC820 alloy, and the necklace structures are formed, thereby demonstrating the occurrence of DRX [23,24]. The necklace structure is a result of the extensive bulging of grain boundaries by local migration, which is the main mechanism of recrystallization nucleation [25]. At elevated temperature, the moving and climbing of dislocations become easy due to the increased additional slip systems via thermal

activation. Thus, the movement of dislocations promotes the DRX. Furthermore, with the decrease in the strain rate from 3 s⁻¹ to 0.01 s⁻¹ at 250 °C, the number of DRXed grains increases and the microstructure appears to be fully recrystallized. The increased temperature and decreased strain rate are beneficial to activating of DRX. Figure 6(c) displays that the DRXed grains evidently grow up and coarsen and then continuously compress at 400 °C and 0.01 s⁻¹. The DRXed grains have adequate time to deform again at the high deformation temperature and low strain rate, thereby resulting in the formation of DRXed-deformed grains. This phenomenon is ascribed to the increased nucleation ratio of recrystallization and high migration of grain boundaries at high temperature and low strain rate [26].

The TEM images of the hot-compressed assolutionized TZC820 alloy at 400 °C and 3 s⁻¹ are presented in Fig. 7. Notably, the fine-DRXed grain area

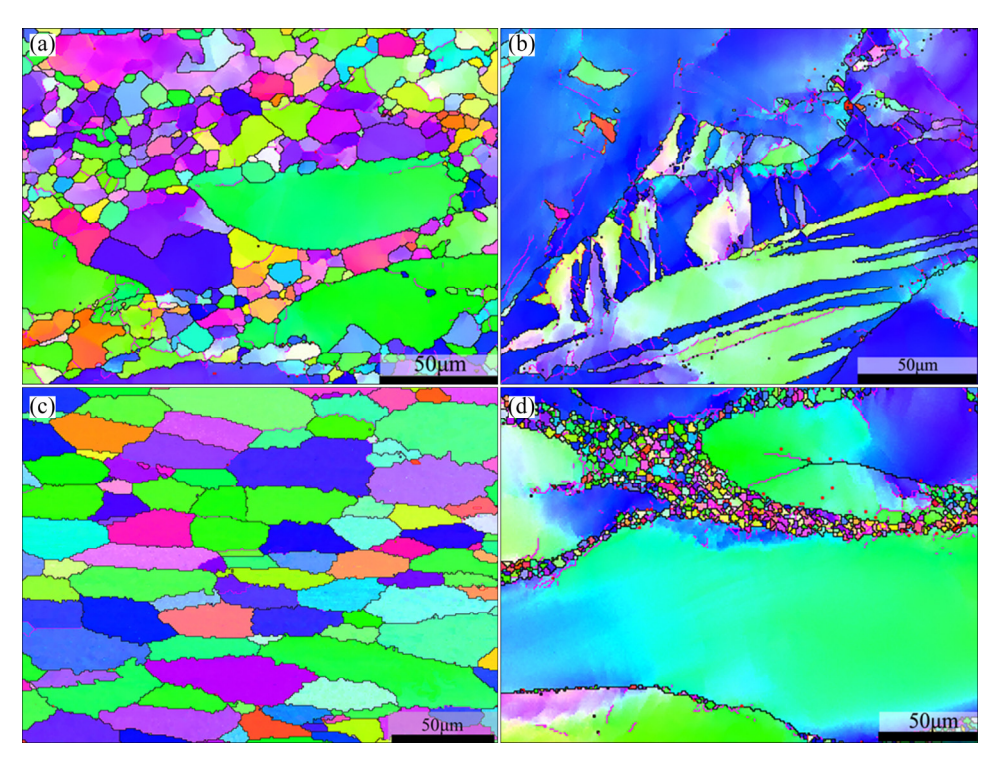


Fig. 6 EBSD orientation maps for TZC820 alloy under various deformation conditions: (a) 250 °C, 0.01 s⁻¹; (b) 250 °C, 3 s⁻¹; (c) 400 °C, 0.01 s⁻¹; (d) 400 °C, 3 s⁻¹

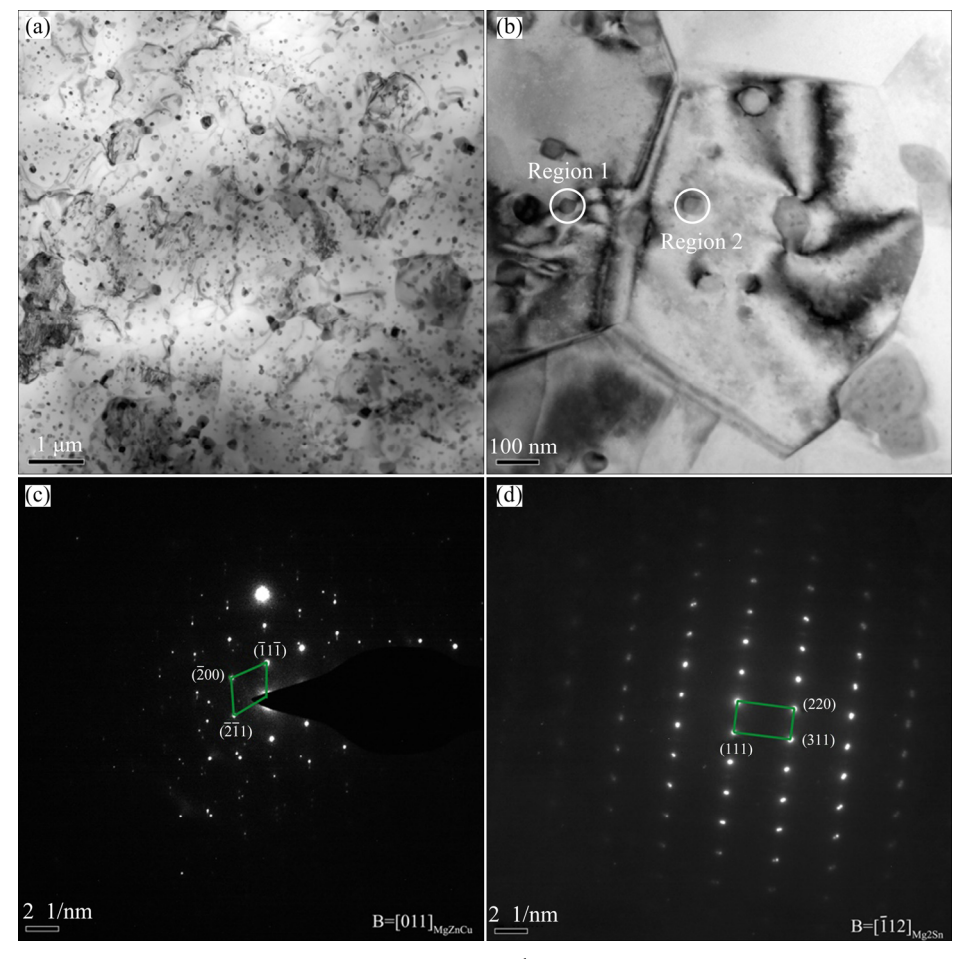


Fig. 7 TEM images of deformed TZC820 alloy at 400 $^{\circ}$ C and 3 s⁻¹: (a) Bright field TEM image of fine-grain region; (b) High magnification TEM image; (c) SAED of Region 1; (d) SAED of Region 2

is selected as the observation region. Figure 7(a) illustrates that numerous fine secondary phases are uniformly distributed in the α -Mg matrix. Moreover, the high magnification TEM image and the SAED of Regions 1 and 2 reveal that the fine secondary phases are composed of broken and precipitated MgZnCu and Mg₂Sn particles, as demonstrated in Figs. 7(b-d). Although the as-cast TZC820 alloy has been subjected to high temperature solution treatment, as exhibited in Fig. 1, the Mg₂Sn and MgZnCu phases can still be observed considering the high content of Sn and limited solid solubility of Cu. A stress concentration is generated and increases rapidly with the occurrence of plastic deformation, thus leading to local cracks around the coarse particles. With further deformation, the secondary phases break into small particles and spheroidize to minimize the surface energy [14]. Moreover, the micron-sized particles and nano-sized precipitates exert comprehensive effects on grain refinement of the deformed alloy. Basal slip and extension twinning can be activated easily due to low critical shear stresses and non-basal slip systems can also be operated at elevated temperature [27]. The broken Mg₂Sn and MgZnCu particles promote the dislocation accumulation in original grains, thereby facilitating the nucleation of new grains; this mechanism is called particle-stimulated nucleation (PSN) mechanism [14]. Furthermore, the nano-sized Mg₂Sn particles play a significant role in pinning grain boundaries and hindering dislocation movement, thus resulting in grain refinement. 3.3.2 Numerical study

Cellular automaton (CA) is a dynamic system with local interactions in which space and time are discrete [13]. The CA method coupled with periodic boundary conditions has been extensively used to evaluate the effect of deformation conditions on the microstructure evolution [28,29]. To study and reconstruct the effect of secondary phases on the DRX behavior during the hot deformation, a CA simulation is conducted to model the DRX for the as-solutionized TZC820 alloy. In the present CA model, the simulation mesh is set to be an 800×800 square lattice in which every cell represents 1 µm of the actual dimension. The following assumptions are utilized in this CA model:

- (1) The initial microstructure is homogenous.
- (2) The dislocation and orientation are uniform within each grain.
- (3) Nucleation occurs on grain boundaries and secondary phases.
- (4) The precipitates are pre-introduced, rather than being introduced during the deformation process.

First, we perform a compression simulation at 250 °C and 0.01 s⁻¹ to verify the accuracy of the CA method. Figure 8 illustrates the initial microstructure of

the as-solutionized TZC820 alloy, the corresponding grain size distribution and the deformed microstructures at strain of 0.4 and 0.9. The various colors, small particles and large particles represent grains with different orientations, precipitates and broken secondary phases, correspondingly. The initial microstructure characterization, including the grain size and secondary phase distribution, coincides with the experimental results (Fig. 2(a)). When the as-solutionized TZC820 alloy is compressed to a strain of 0.4, some DRXed grains appear, and the DRXed grains initially nucleate at the grain boundaries of the deformed grains in the initial microstructure, as depicted in Fig. 8(c). The volume fraction of DRXed grains increases when the compression strain increases to 0.9, but some deformed grains still remain in the microstructure (Fig. 8(d)). This result is consistent with the result demonstrated in Fig. 6(a).

3.4 Processing map

The processing map, which is based on the dynamic material model (DMM), has been extensively used to optimize the processing parameters and predict the suitable domains of many alloys in terms of the various microstructural characteristics in different deformation conditions [30,31]. The microstructure evolution during hot deformation can be expressed as the efficiency of power dissipation (η) [21]:

$$\eta = \frac{2m}{m+1} \tag{3}$$

where m is the strain rate sensitivity parameter, which is determined by $\ln \sigma - \ln \varepsilon$ [20]. Generally, a high efficiency of power dissipation improved the workability of the metal. However, a large efficiency of power dissipation may cause the recrystallized grains to be coarse and even induce cracks in the deformed body. Therefore, the instability map is developed and can be characterized using an instability criterion, which is based on the extremum principles of entropy production, and this criterion is expressed as follows [32]:

$$\xi(\dot{\varepsilon}) = \frac{\partial \ln[m/(m+1)]}{\partial \ln \dot{\varepsilon}} + m < 0 \tag{4}$$

where $\xi(\varepsilon)$ is the instability parameter. In Eq. (4), the instability map varies with the strain rate and temperature, and the negative value of $\xi(\dot{\varepsilon})$ indicates the instability flow. Finally, the processing map can be constructed by merging the power dissipation map and the instability maps.

The processing maps for the as-solutionized TZC820 alloy at the true strain of 0.2, 0.4, 0.6 and 0.8 are developed, as displayed in Fig. 9. In this figure, the contour numbers represent the efficiency of power

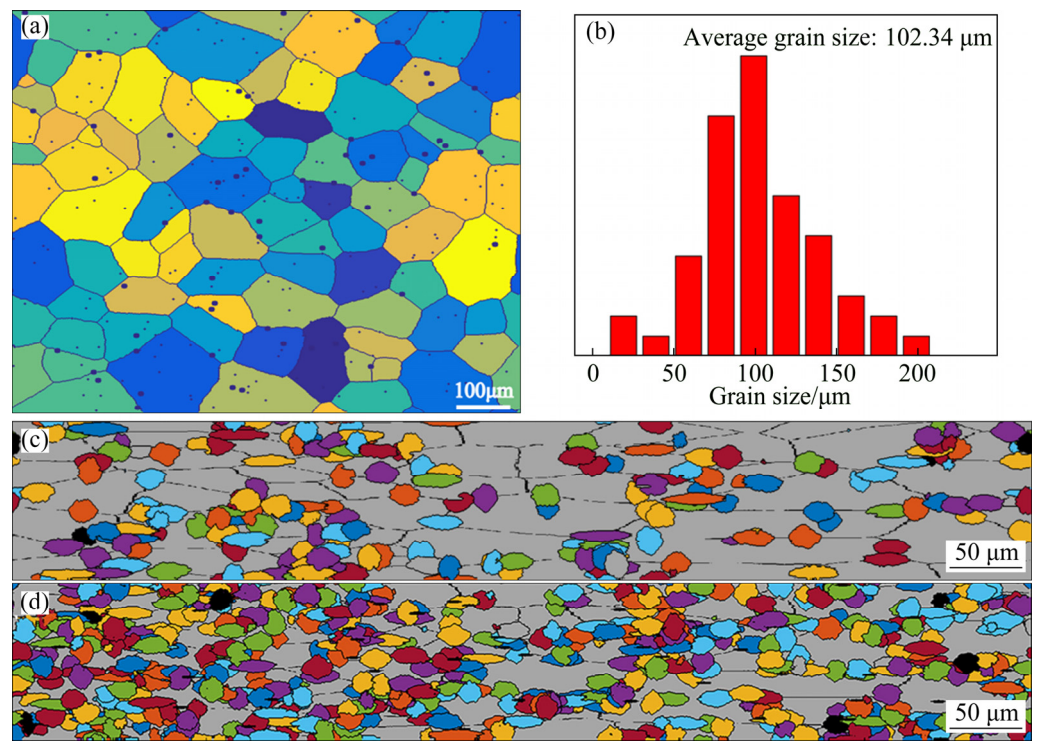


Fig. 8 Microstructural evolution of as-solutionized TZC820 alloy during compression deformation at 250 °C and 0.01 s⁻¹ using CA simulation: (a) Initial microstructure; (b) Corresponding grain size distribution; (c) At strain of 0.4; (d) At strain of 0.9

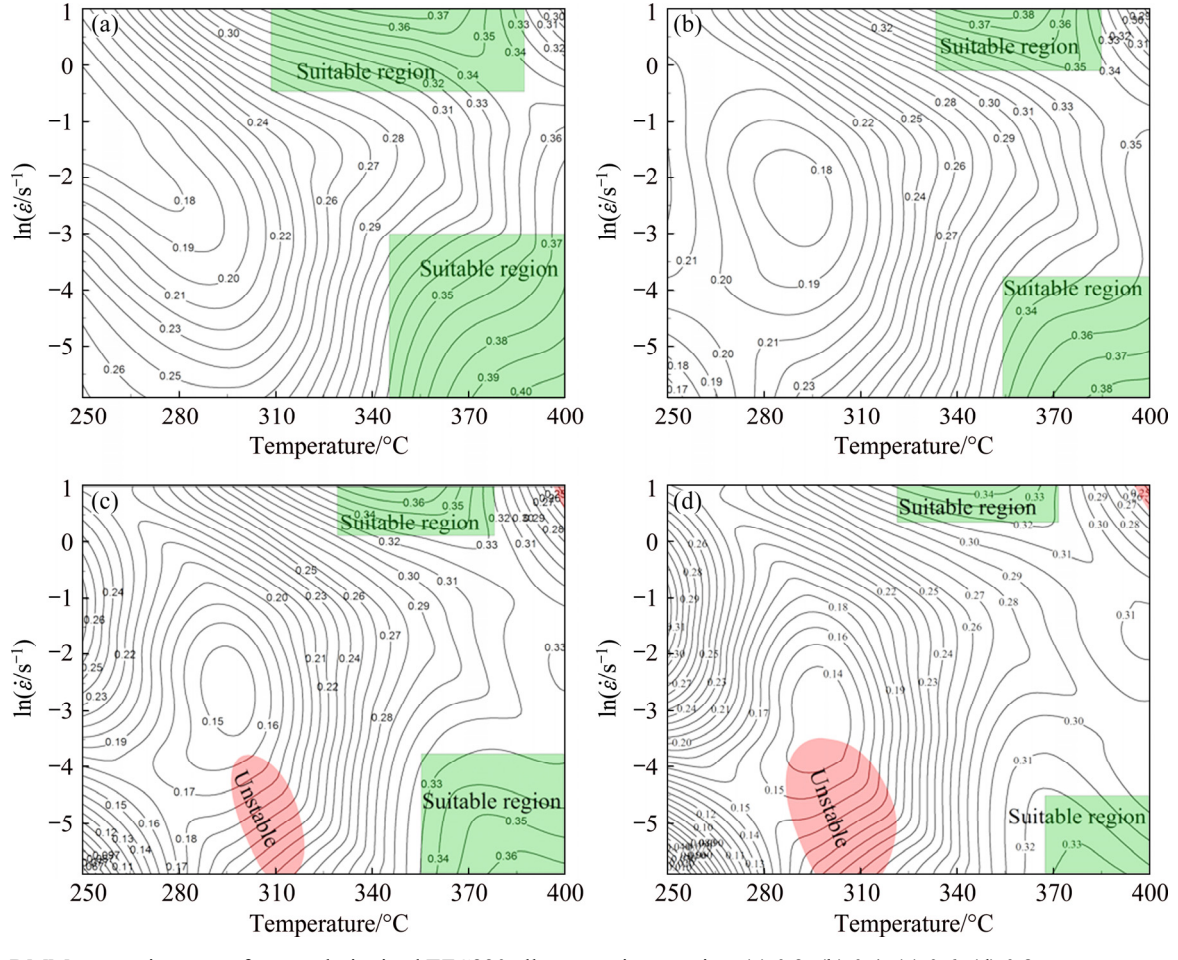


Fig. 9 DMM processing maps for as-solutionized TZC820 alloy at various strains: (a) 0.2; (b) 0.4; (c) 0.6; (d) 0.8

dissipation, and the red areas indicate the instability domains. The efficiency of power dissipation decreases with the increase in strain rate and the decrease in deformation temperature. The low efficiency of power dissipation indicates that the deformation energy is mostly used for activating the slip system and the dislocation movement rather than promoting the microstructure evolution [33]. In addition, the strain significantly affects the efficiency of power dissipation and instability domain. When the strain is 0.2 or 0.4, no flow instability region appears, and the high efficiency of power dissipation area is narrowed with the increase in strain. However, when the strain increases up to 0.6 and 0.8, flow instability occurs at 290-320 °C with the stain rate of 0.01–0.1 s⁻¹. In addition, flow instability can also occur even at high temperature and high strain rate. This condition is attributed to the limited time for dynamic recrystallization and the strong work hardening effect. Thus, the strain rate of the hot deformation of the as-solutionized TZC820 alloy cannot be extensively

In summary, flow instability occurs during hot deformation of the as-solutionized TZC820 alloy at a middle temperature and low strain rate and/or high temperature and strain rate. However, processing efficiency maps show that the processing efficiency is high at high temperature, but decreases with the increase in strain rate. The analysis shows that the optimum deformation parameters for the as-solutionized TZC820 alloy are under the condition of high temperature and relatively low strain rate, and middle temperature and high strain rate. These conditions occur at 370–400 °C and strain rate of 0.01 s⁻¹, and at 320–360 °C and strain rates of 1–3 s⁻¹.

4 Conclusions

- (1) The flow behavior of the as-solutionized TZC820 alloy is significantly influenced by strain rate and temperature. The flow stress decreases with the decrease in strain rate and the increase in temperature. Moreover, the strain significantly influences the flow behavior of the alloy.
- (2) Strain rate and deformation temperature significantly affect the microstructure evolution of the as-solutionized TZC820 alloy in hot deformation. The increase in deformation temperature and the decrease in strain rate promote DRX and the growth of DRX grains. Moreover, DRX grains evidently grow and coarsen, and continuously compress at 400 °C and 0.01 s⁻¹.
- (3) The established processing maps are sensitive to strains in which the region of flow instability increases and the region of optimum processing condition decreases. The optimum processing parameters for hot

workability of TZC820 alloy are obtained at 370–400 °C and strain rate of 0.01 s⁻¹, and at 320–360 °C and strain rates of 1-3 s⁻¹.

References

- [1] SU Min-liang, ZHANG Jing-huai, FENG Yan, BAI Yi-jia, WANG Wei, ZHANG Zhong-wu, JIANG Feng-chun. Al-Nd intermetallic phase stability and its effects on mechanical properties and corrosion resistance of HPDC Mg-4Al-4Nd-0.2Mn alloy [J]. Journal of Alloys and Compounds, 2017, 691: 634-643.
- [2] ZHANG Yang, CHEN Xiao-yang, LU Ya-lin, LI Xiao-ping. Microstructure and mechanical properties of as-extruded Mg-Sn-Zn-Ca alloy with different extrusion ratios [J]. Transactions of Nonferrous Metals Society of China, 2018, 28(11): 2190-2198.
- [3] CHANG Li-li, SHI Chun-chang, CUI Hong-wei. Enhancement of mechanical properties of duplex Mg-9Li-3Al alloy by Sn and Y addition [J]. Transactions of Nonferrous Metals Society of China, 2018, 28(1): 30-35.
- [4] ZHANG Jing-huai, LIU Shu-juan, WU Rui-zhi, HOU Le-gan, ZHANG Mi-lin. Recent developments in high-strength Mg-REbased alloys: Focusing on Mg-Gd and Mg-Y systems [J]. Journal of Magnesium and Alloys, 2018, 6(3): 277-291.
- [5] MENDIS C L, BETTLES C J, GIBSON M A, HUTCHINSON C R. An enhanced age hardening response in Mg-Sn based alloys containing Zn [J]. Materials Science and Engineering A, 2006, 435-436: 163-171.
- [6] SASAKI T T, OH-ISHI K, OHKUBO T, HONO K. Enhanced age hardening response by the addition of Zn in Mg-Sn alloys [J]. Scripta Materialia, 2006, 55: 251-254.
- [7] LIU Chao-qiang, CHEN Hou-wen, NIE Jian-feng. Interphase boundary segregation of Zn in Mg-Sn-Zn alloys [J]. Scripta Materialia, 2016, 123: 5-8.
- [8] HUANG X F, ZHANG W Z. Improved age-hardening behavior of Mg-Sn-Mn alloy by addition of Ag and Zn [J]. Materials Science and Engineering A, 2012, 552: 211-221.
- [9] SASAKI T T, YAMAMOTO K, HONMA T, KAMADO S, HONO K. A high-strength Mg-Sn-Zn-Al alloy extruded at low temperature [J]. Scripta Materialia, 2008, 59: 1111-1114.
- [10] SON H T, LEE J B, JEONG H G, KONNO T J. Effects of Al and Zn additions on mechanical properties and precipitation behaviors of Mg–Sn alloy system [J]. Materials Letters, 2011, 65: 1966–1969.
- [11] PAN Hu-cheng, QIN Gao-wu, XU Ming, FU He, REN Yu-ping, PAN Fu-sheng, GAO Zheng-yuan, ZHAO Chao-yong, YANG Qing-shan, SHE Jia, SONG Bo. Enhancing mechanical properties of Mg–Sn alloys by combining addition of Ca and Zn [J]. Materials and Design, 2015, 83: 736–744.
- [12] NAKATA T, XU C, AJIMA R, SHIMIZU K, HANAKI S, SASAKI T T, MA L, HONO K, KAMADO S. Strong and ductile age-hardening Mg-Al-Ca-Mn alloy that can be extruded as fast as aluminum alloys [J]. Acta Materialia, 2017, 130: 261-270.
- [13] ELSAYED F R, SASAKI T T, OHKUBO T, TAKAHASHI H, XU S W, KAMADO S, HONO K. Effect of extrusion conditions on microstructure and mechanical properties of microalloyed Mg-Sn-Al-Zn alloys [J]. Materials Science and Engineering A, 2013, 588: 318-328.
- [14] WANG Yong-jian, PENG Jian, ZHONG Li-ping. On the microstructure and mechanical property of as-extruded Mg-Sn-Zn alloy with Cu addition [J]. Journal of Alloys and Compounds, 2018, 744: 234-242.
- [15] LV Bin-jiang, PENG Jian, WANG Yong-jian, AN Xiao-qin, ZHONG Li-ping, TANG Ai-tao, PAN Fu-sheng. Dynamic recrystallization behavior and hot workability of Mg-2.0Zn-0.3Zr-0.9Y alloy by

- using hot compression test [J]. Materials and Design, 2014, 53: 357-365.
- [16] CHEN Xi-hong, FAN Cai-he, HU Ze-yi, YANG Jian-jun, GAO Wen-li. Flow stress and dynamic recrystallization behavior of Al-9Mg-1.1Li-0.5Mn alloy during hot compression process [J]. Transactions of Nonferrous Metals Society of China, 2018, 28(12): 2401-2409.
- [17] HADADZADEH A, WELLS M A. Analysis of the hot deformation of ZK60 magnesium alloy [J]. Journal of Magnesium and Alloys, 2017, 5(4): 369–387.
- [18] KOUNDINYA N T B N, RAMAN L, NANDHA K, CHAWAKE N, KOTTADA R S. Hot deformation behaviour of Mg-3Al-3Sn and Mg-3Al-3Sn-1Zn alloys: Role of Zn [J]. Materialia, 2018, 3: 274-287.
- [19] WU H, WEN S P, HUANG H, WU X L, GAO K Y, WANG W, NIE Z R. Hot deformation behavior and constitutive equation of a new type Al-Zn-Mg-Er-Zr alloy during isothermal compression [J]. Materials Science and Engineering A, 2016, 651: 415-424.
- [20] WANG Yong-jian, PENG Jian, ZHONG Li-ping, PAN Fu-sheng. Modeling and application of constitutive model considering the compensation of strain during hot deformation [J]. Journal of Alloys and Compounds, 2016, 681: 455–470.
- [21] PENG Jian, WANG Yong-jian, ZHONG Li-ping, PENG Long-fei, PAN Fu-sheng. Hot deformation behavior of homogenized Al-3.2Mg-0.4Er aluminum alloy [J]. Transactions of Nonferrous Metals Society of China, 2016, 26(4): 945-955.
- [22] SU Ze-xing, WAN Li, SUN Chao-yang, CAI Yun, YANG Dai-jun. Hot deformation behavior of AZ80 magnesium alloy towards optimization of its hot workability [J]. Materials Characterization, 2016, 122: 90–97.
- [23] SAMANTARAY D, MANDAL S, JAYALAKSHMI M, ATHREYA C N, BHADURI A K, SUBRAMANYA S V. New insights into the relationship between dynamic softening phenomena and efficiency of hot working domains of a nitrogen enhanced 316L(N) stainless steel [J]. Materials Science and Engineering A, 2014, 598: 368–375.
- [24] SHI Zhao-xia, YAN Xiao-feng, DUAN Chun-hua. Characterization of hot deformation behavior of GH925 superalloy using constitutive

- equation, processing map and microstructure observation [J]. Journal of Alloys and Compounds, 2015, 652: 30–38.
- [25] MOMENI A, ABBASI S M, MORAKABATI M, BADRI H, WANG X. Dynamic recrystallization behavior and constitutive analysis of Incoloy 901 under hot working condition [J]. Materials Science and Engineering A, 2014, 615: 51–60.
- [26] ZHOU Zhao-hui, FAN Qi-chao, XIA Zhi-hui, HAO Ai-guo, YANG Wen-hua, JI Wei, CAO Hai-qiao. Constitutive relationship and hot processing maps of Mg-Gd-Y-Nb-Zr alloy [J]. Journal of Materials Science and Technology, 2017, 33(7): 637-644.
- [27] BAJARGAN G, SINGH G, SIVAKUMAR D, RAMAMURTY U. Effect of temperature and strain rate on the deformation behavior and microstructure of a homogenized AZ31 magnesium alloy [J]. Materials Science and Engineering A, 2013, 579: 26–34.
- [28] ZHANG Tao, LU Shi-hong, WU Yun-xin, GONG Hai. Optimization of deformation parameters of dynamic recrystallization for 7055 aluminum alloy by cellular automaton [J]. Transactions of Nonferrous Metals Society of China, 2017, 27(6): 1327–1337.
- [29] LIU Yan-xing, LIN Y C, LI Hong-bin, WEN Dong-xu, CHEN Xiao-min, CHEN Ming-song. Study of dynamic recrystallization in a Ni-based superalloy by experiments and cellular automaton model [J]. Materials Science and Engineering A, 2015, 626: 432–440.
- [30] DUAN Yong-hua, MA Li-shi, QI Hua-rong, LI Run-yue, LI Ping. Developed constitutive models, processing maps and microstructural evolution of Pb-Mg-10Al-0.5B alloy [J]. Materials Characterization, 2017, 129: 353–366.
- [31] XU C, PAN J P, NAKATA T, QIAO X G, CHI Y Q, ZHENG M Y, KAMADO S. Hot compression deformation behavior of Mg-9Gd-2.9Y-1.9Zn-0.4Zr-0.2Ca (wt%) alloy [J]. Materials Characterization, 2017, 124: 40-49.
- [32] WU Yu-ting, LIU Yong-chang, LI Chong, XIA Xing-chuan, HUANG Yu-an, LI Hui-jun, WANG Hai-peng. Deformation behavior and processing maps of Ni₃Al-based superalloy during isothermal hot compression [J]. Journal of Alloys and Compounds, 2017, 712: 687–695.
- [33] WU Horng-yu, WU Cheng-tao, YANG Jie-chen, LIN Ming-jie. Hot workability analysis of AZ61 Mg alloys with processing maps [J]. Materials Science and Engineering A, 2014, 607: 261–268.

一种新型 Mg-8Sn-2Zn-0.5Cu 合金 热加工变形的组织演变和优化参数分析

钟丽萍 1,2, 王永建 1,2

- 1. 四川轻化工大学 材料科学与工程学院, 自贡 643000;
- 2. 四川轻化工大学 材料腐蚀与防护四川省重点实验室, 自贡 643000

摘 要:利用 Gleeble-1500D 热模拟试验机在 250~400 °C、 $0.01~3~s^{-1}$ 变形条件下,通过实验和模拟研究固溶 Mg-8Sn-2Zn-0.5Cu(TZC820)合金的热变形行为。结果表明,变形温度和应变速率对合金的流变应力和材料常数有显著的影响。此外,基于真实应力-应变曲线建立应变补偿的本构关系。合金的主要变形机制为动态再结晶(DRX),随着变形温度的升高和应变速率的降低,DRX 程度得到明显提高。利用元胞自动机方法模拟该合金在热压缩过程中的显微组织演变。此外,构建合金的塑性加工图,得到固溶态 TZC820 合金的较优加工条件为 370~400 °C、 $0.01~s^{-1}$ 和 320~360 °C、 $1-3~s^{-1}$ 。

关键词: Mg-8Sn-2Zn-0.5Cu 合金; 热变形; 动态再结晶; 加工图